

CHARACTERIZATION OF THE LOCAL DEFORMATION BEHAVIOR OF ALUMINUM MATRIX COMPOSITES BY IN SITU SEM METHODS

Schuff, Sebastian^{1,*}; Balle, Frank¹; Fitschen, Jan Henrik²; Beck, Tilmann¹; Eifler, Dietmar¹; Steidl, Gabriele²

¹ Institute of Materials Science and Engineering (WKK), University of Kaiserslautern,
P.O. Box 3049, 67653 Kaiserslautern
<https://www.mv.uni-kl.de/wkk/wkk/schuff@mv.uni-kl.de>

² Department of Mathematics, University of Kaiserslautern,
P.O. Box 3049, 67653 Kaiserslautern
<http://www.mathematik.uni-kl.de/imagepro/mainpage/fitschen@mathematik.uni-kl.de>

Keywords: Aluminum matrix composite, AMC, In situ testing, Local mechanical properties, Microstructure, Image analysis

ABSTRACT

In the automotive and aerospace industry, the use of lightweight alloys is continuously increasing. However, classical aluminum alloys cannot fulfill all demands of improved future lightweight concepts. One possibility to overcome this issue is to reinforce a ductile metallic matrix with a second phase like fibers, whiskers or particles, i.e. producing metal matrix composites (MMC) or aluminum matrix composites (AMC) for innovative engineering applications. The main advantage of these multiphase materials is an increase of specific mechanical properties with respect to the matrix alloy, e.g. Young's modulus and ultimate tensile strength (UTS). In addition, the composite mass density remains close to the matrix alloy due to relatively low volume contents of reinforcement like Al₂O₃, SiO₂ or SiC. In contrast, the improved stiffness as well as the possibility to use further strengthening mechanisms of the metallic phase, such as precipitation hardening, leads to an increase of the global mechanical properties. The deformation capability and damage mechanisms are strongly affected by the matrix / reinforcement interaction. Especially local deformations caused by this pronounced heterogeneity are often not taken into account during the engineering design of AMC components. The present study focuses on AMC variants reinforced by SiC particles with a nominal volume content of 17 % and a varying size from nominal 0.3 μm to 3 μm. Micro-mechanical tests on notched samples were realized using an in situ tension-compression load frame mounted in a SEM. Micrograph sequences determined under increasing mechanical load up to final failure are the basis for computation of the strain tensor by mathematical image analysis. This procedure is used to monitor and analyze the arrangement of the multiphase microstructure and its changes at the surface during mechanical loading. Especially the size of the SiC particles as an influencing factor is discussed for monotonic properties of AMC.

1 INTRODUCTION

In the recent years, especially in the automotive and aerospace industry, the use of lightweight alloys constantly increased due to a continuing demand for weight reduction of engineering components. However, these alloys cannot fulfill all demands of improved design requirements, i.e. an optimal compromise between strength and ductility. This issue can at least be partially overcome, if a ductile metallic matrix is reinforced by a second phase like particles or fibers to enlarge the field of different application possibilities [1–5]. Such materials are in general called metallic matrix composites (MMC) and, in the special case of aluminum matrix alloys, aluminum matrix composites (AMC) [6]. Potential applications are e.g. cylinder sliding surfaces in car engines. High performance Formula 1 conrods were also manufactured of aluminum alloy AA 2124 reinforced with 25 vol.-% ultra-fine silicon carbide

particles. Fan bypass structures in aero engines with maximum service temperature below 150 °C are further potential applications for AMC components.

An improvement of specific macroscopic mechanical properties, e.g. ultimate tensile strength (UTS), Young's modulus and fatigue resistance, compared to the unreinforced matrix alloy is the main advantage of MMCs. Different reinforcing materials are chosen with a comparable mass density of the matrix. In case of Al_2O_3 , SiC, SiO_2 or B_4C the overall composite density remains close to the matrix alloy [7, 8]. Furthermore, the possibility to use strengthening mechanisms of the matrix alloy, such as precipitation hardening in case of aluminum alloys, leads to a further increase of macroscopic mechanical strength [9]. The deformation capability and damage mechanisms are strongly affected by the matrix / reinforcement interaction due to pronounced differences in stiffness. These local heterogeneities are often not taken into account during the engineering design process of AMC components, e.g. finite element method (FEM) based simulations [10].

In the present work, the local mechanical properties of AMC with varying SiC particle size were investigated. The macroscopic mechanical properties of three different composite materials were determined by monotonic tensile tests according to DIN EN ISO 6892-1 using a specimen geometry defined in DIN 50125. Furthermore, micro-mechanical tensile tests were realized by an in situ tension-compression load frame (Kammrath & Weiss Co.) mounted in a scanning electron microscope (SEM). SEM image sequences of specific positions on the specimen's surface were used for the computation of local deformation determined under increasing mechanical load up to final fracture.

2 ALUMINUM MATRIX COMPOSITES

The present work focuses on AMC manufactured by powder metallurgy and supplied as cylindrical bars with a diameter of 25 mm by Aerospace Metal Composites Ltd., Farnborough (United Kingdom). As matrix alloy, the high quality aerospace grade wrought aluminum alloy AA 2124 (AlCu4Mg1), with the main alloying elements copper and magnesium, is used. This alloy is reinforced with SiC particles with a nominal volume content of 17 % given by the manufacturer.

Powder metallurgy and mechanical alloying technique are used to consolidate matrix alloy and reinforcement phase. Process conditions during high energy mixing of both components are controlled to produce a macroscopic uniform distribution of these SiC particles. This powder mixture is compacted to billets by hot isostatic pressing. Billets are further processed by extrusion techniques. This leads to a preferred orientation of the SiC particles in extrusion direction (ED). The extruded bars were finally heat treated to condition T6 and to achieve high strength by precipitation hardening and artificial aging.

In this study, composites with three different sizes of SiC particles were investigated. The nominal particle size, as given by the manufacturer, decreases from 3.0 μm (AMC 217xe) over 0.7 μm (AMC xfine217) to 0.3 μm (AMC xxfine217). Table 1 shows the results of the chemical analysis of the delivered batches.

Al	Cu	Mg	Mn	Fe	Zn	Si	Ti	Cr
base	3.8 – 4.9	1.2 – 1.8	0.3 – 0.9	< 0.3	< 0.25	< 0.2	< 0.2	< 0.1

Table 1: Chemical analysis of Al-matrix in weight-%

A comparison of the microstructures of the investigated AMC variants is shown in Figure 1. The surface of the longitudinal sections is mechanically polished. The aluminum matrix appears in gray in the SEM micrographs, the SiC particles in bright and isolated pores correspond to black areas (marked by red circles). Furthermore, dotted black lines mark particle free zones (PFZs) elongated in ED. Besides this, a preferred orientation of the SiC particles in ED is obvious.

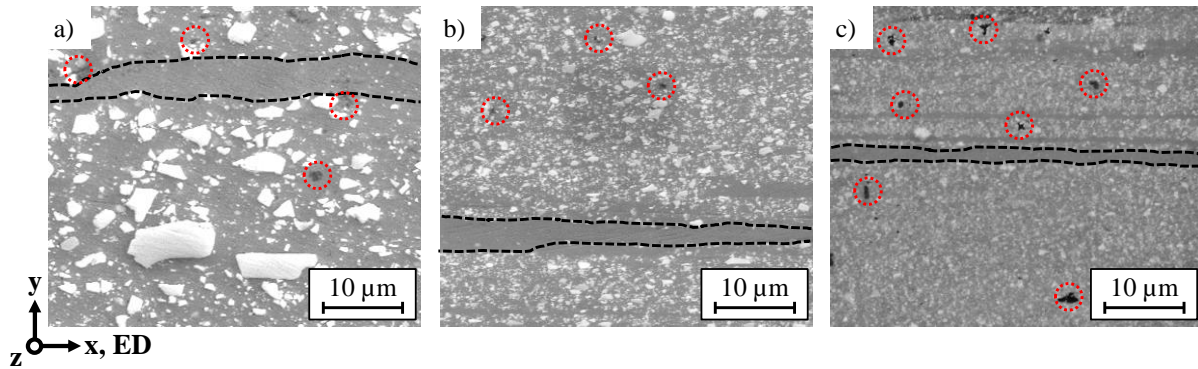


Figure 1: Microstructure of a) AMC 217xe, b) AMC xfine217 and c) AMC xxfine217

3 EXPERIMENTAL SETUP

3.1 Specimen geometries

The extruded bars were machined by wire spark erosion to the applied flat specimen geometries according to DIN 50125 for conventional ex situ tensile tests while smaller notched samples were used for in situ tensile testing in the SEM. All surfaces of each specimen type were polished to avoid crack initiation at machining induced surface defects. The top and bottom side of each specimen were mechanically prepared by grinding wheels and polishing cloths. In contrast, the notched surfaces were manually prepared with abrasive paper and diamond suspension. Due to the dimensions of the extruded bars, the longitudinal axis of each specimen type corresponds to the extrusion direction. Flat specimens for ex situ tensile tests are named E 4x10x35 according to DIN 50125. They have a gauge length of 35 mm, a thickness of 4 mm and a width of 10 mm.

In situ experiments were performed with the specimen geometry shown in Figure 2. The name for this geometry is given according to the notch factor of $\alpha_K = 1.1$ determined by elastic FEM simulation. The overall length is 65.0 mm, the width is 10.8 mm and the thickness is 3.5 mm. The notch with radii of 4.4 mm was applied to limit the area affected by major microstructural changes during in situ experiments to the notch root. An extensometer clamped close to the upper and lower end of the notched area (see Figure 2) was used for strain measurement. Note that the extensometer strain without correction for notch effects is given in the evaluations of tensile tests in the following sections.

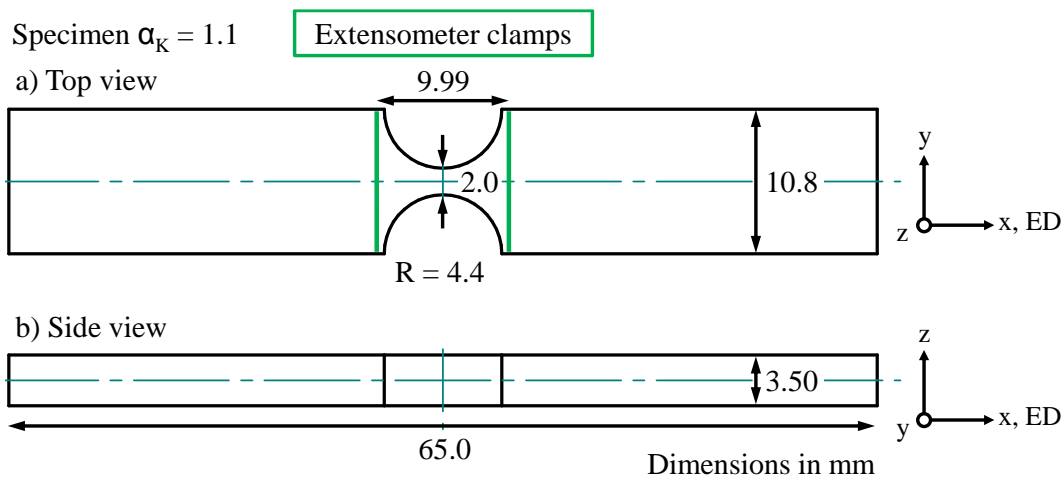


Figure 2: Notched specimen ($\alpha_K = 1.1$) for micro-mechanical in situ testing; a) top view, b) side view

3.2 Macroscopic monotonic tensile tests

Monotonic tensile tests were performed using an electromechanical tensile testing system (Zwick Z250) to determine macroscopic mechanical properties of all investigated AMC variants. Young's modulus in the direction of extrusion, 0.2 % yield strength, UTS and elongation at fracture were identified during four experiments per AMC variant.

3.3 In situ deformation tests

Micro-mechanical tests at small notched specimens (see Figure 2) were realized using an in situ tension-compression load frame (Kammrath & Weiss Co.) mounted in an FEI Quanta 600 FEG SEM. A macroscopic view of a mounted specimen $\alpha_K = 1.1$ is shown in Figure 3 a. The extensometer clamps are attached to the backside of the specimen. Position 1 to 3 represent selected areas at the top side of the specimen given in Figure 3 b. Furthermore, the stage of the SEM is tilted about 30° to track microstructural changes also in the notch root area (positions 4 to 6). Tilt correction of all micrographs is applied directly within the software of the SEM. Additionally, SEM images taken at each position are stored with at least two different magnifications to study the impact of SiC particle size.

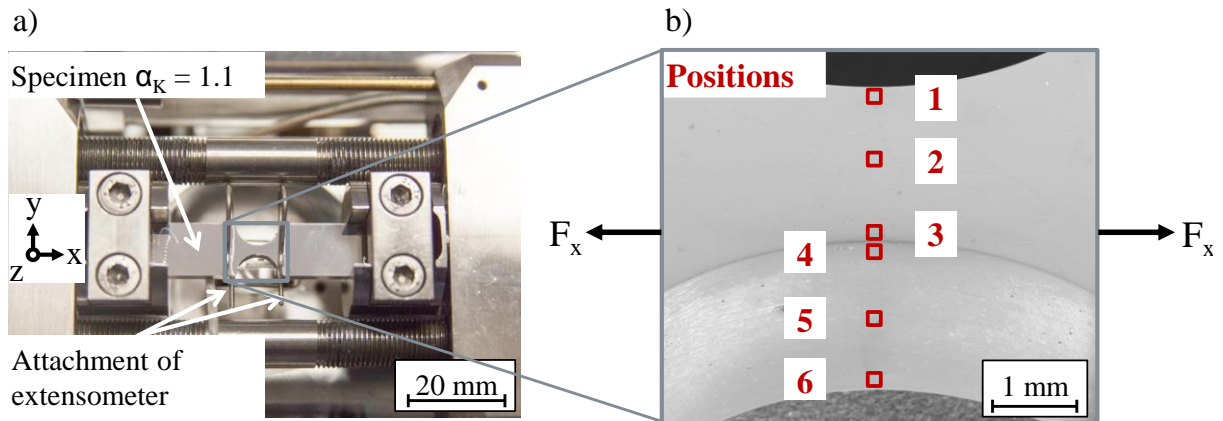


Figure 3: a) Experimental setup of an in situ deformation test with specimen $\alpha_K = 1.1$ and b) areas of interest (positions 1- 6)

Micrographs of all positions on the specimen's surface determined under increasing mechanical load up to final failure are the basis for the computation of local deformation.

3.4 Mathematical image analysis

The analysis of the local deformation during in situ loading experiments is performed by mathematical image analysis [11, 12]. As input data, the micrographs are used to calculate the displacement from a reference image in the unloaded state to the same initial position with applied load. Computation of the displacement field u

$$u := (u_1, u_2)^T \quad \text{Eq. (1)}$$

is done by a variational model for each pixel in the micrograph sequence. This describes the motion of each individual dot from one image to another. In image processing, optical flow is known as the displacement u between image frames. The component u_1 of the vector u corresponds to ED which is parallel to the loading direction while u_2 stands for a displacement perpendicular to the loading direction.

In general, the strain tensor ε is defined via the Jacobian of the displacement field u for deformations of a continuum body by

$$\varepsilon = \begin{pmatrix} \varepsilon_{11} & \varepsilon_{12} \\ \varepsilon_{21} & \varepsilon_{22} \end{pmatrix} := \frac{1}{2}(\nabla u + \nabla u^T) = \begin{pmatrix} \partial_x u_1 & \frac{1}{2}(\partial_y u_1 + \partial_x u_2) \\ \frac{1}{2}(\partial_y u_1 + \partial_x u_2) & \partial_y u_2 \end{pmatrix} \quad \text{Eq. (2)}$$

The proposed variational model for calculating the strain tensor is mainly based on two assumptions: The first assumption is a constant gray value of corresponding pixels. Hence, local deformation is considered being the reason for changes in gray value. The second assumption states that the Jacobian can be split in a so called smooth and non-smooth part. Global effects related to the entire area of the observed image are represented by the smooth part while the non-smooth part represents an emphasized view on local phenomena, e.g. micro-cracks. The combination of smooth and non-smooth part is used to highlight damages with high sensitivity by the calculated derivatives $\partial_x u_1$ and $\partial_y u_2$. In the proposed method, local phenomena, especially material separation, have to be removed for a correct description of the strain field. Because of that, the calculated strain tensor a is defined as

$$a = \begin{pmatrix} a_{11} & a_{12} \\ a_{21} & a_{22} \end{pmatrix} \quad \text{Eq. (3)}$$

corresponding to the strain tensor ε described above but not considering the non-smooth part. Further details are given in [12].

The strain tensor is directly calculated in an iteration process by the developed algorithm. Compared to commercial digital image correlation (DIC) software, this novel method provides strain distributions with higher accuracy and resolves local phenomena much better [12].

4 RESULTS AND DISCUSSION

4.1 Macroscopic material properties

The mechanical properties of an AMC with varying size of SiC particles were determined by monotonic ex situ tensile tests. Table 2 summarizes the results of the experiments related to DIN EN ISO 6892-1 with tensile specimen geometry E 4x10x35, which are in good accordance with literature [13, 14].

	Young's modulus in GPa	0.2 % Yield strength in MPa	UTS in MPa	Elongation at fracture in %
AMC 217xe T6	98.8 ± 6.2	344.2 ± 22.3	489.1 ± 15.9	3.9 ± 0.6
AMC xfine217 T6	98.8 ± 7.5	402.9 ± 17.0	520.4 ± 21.7	2.1 ± 0.4
AMC xxfine217 T6	101.6 ± 3.8	472.7 ± 23.6	533.5 ± 18.8	2.0 ± 0.5
AA 2124 T4 [15]	72.5	300	450	22.0
SiC [16, 17]	400 – 455	-	500	0.12

Table 2: Selected monotonic properties of the composite materials and their single phases

4.2 Damage types of AMC

As mentioned above, the present study focuses on the notched specimen geometry $\alpha_K = 1.1$ to enable an observation of the areas of interest during in situ SEM experiments. Selected micrographs of all explained positions taken at several loadings up final failure are the basis for interpretation of all damage types.

The stress-strain curve of an in situ tensile test of AMC 217xe is given in Figure 4. Discontinuities

indicate interruption of the experiment for surface inspection by scanning electron microscopy. The micrographs taken at the center positions on each surface side show characteristic damage types occurring in AMC. Slip marks (A) can be recognized at the surface due to plastic deformation. This damage type has been often observed, when two SiC particles are close together or in front of the crack tip as indicated at position 2 (Figure 4 a) and position 5 (Figure 4 b). Decoherions (B) at the interface between single SiC particles and aluminum matrix are visible in both micrographs. Under progressive loading, slip marks and decoherions grow together within the aluminum matrix to micro cracks (D) up to specimen failure. This damage type is mostly limited to position 5, corresponding to the elevated local strains at the notch root. Finally, also particle cracking (C) was observed as one further type of damage.

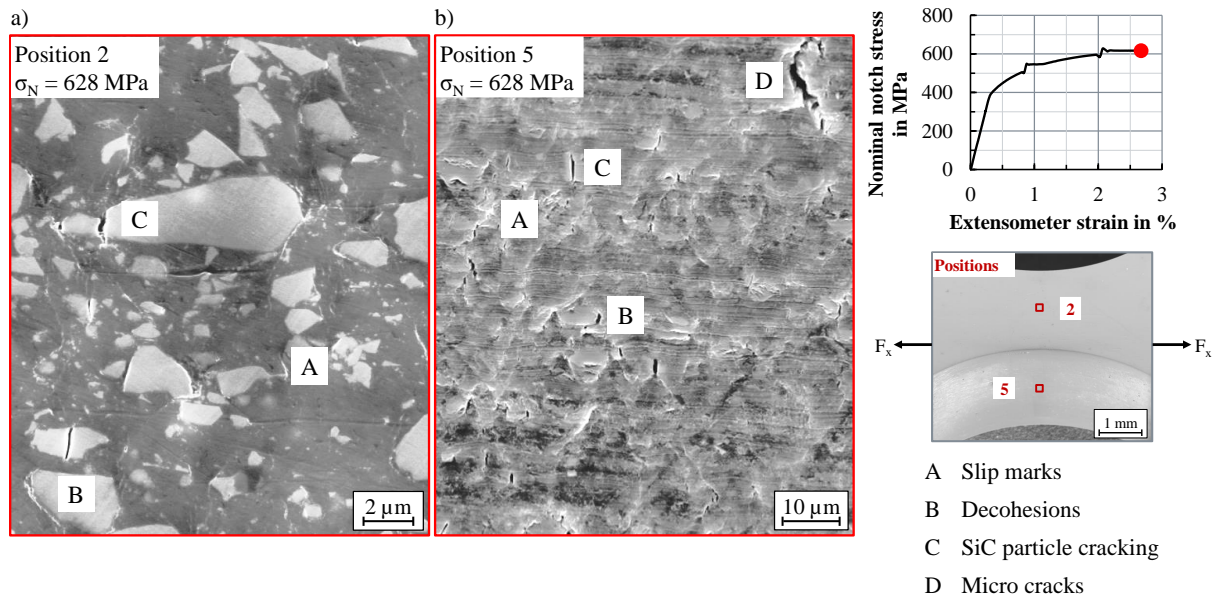


Figure 4: Observed damage types on the surface for loading, exemplarily shown for AMC 217xe ($\alpha_K = 1.1$) at 628 MPa nominal notch stress; a) position 2, b) position 5

Similar results are discussed in [18–22].

4.3 In situ deformation behavior and mathematical image analysis

Mathematical image analysis as outlined in section 3.4 and described in more detail in [12] was applied to in situ tensile tests at all AMC variants. The heterogeneous microstructure helps to assign ongoing damage processes to specific positions within the micrograph and thus to identify the local damage mechanism. Selected results for AMC 217xe are given in Figure 5 to Figure 7 from the same experiment and at the same surface positions as shown in Figure 4. A comparison of calculated strains a_{11} in loading direction is given in Figure 8 for all AMC variants.

A comparison of the calculated local strains a_{11} in loading direction for position 2 and 5 is given together with the respective original SEM images in Figure 5. Micrographs were taken at 505 MPa nominal notch stress, i.e. shortly after onset of macroscopic plastic deformation and less overall stress than the 628 MPa load state considered in Figure 4. For comparability, the same magnification is used for both positions. Therefore, the area of position 2 in Figure 4 a is highlighted in Figure 5 a1. It is clearly visible, that highest strain concentrations occur at position 5. In this area, independent of the AMC variant, first microstructural damage is detected and becomes visible in the calculated a_{11} strain distribution. This correlates well with Figure 4 where a micro crack is obvious at the position marked with D. Note that at the same position a strain concentration is already measurable by mathematical image analysis in Figure 5 b2 although no significant damage can be seen in the corresponding micrograph (Figure 5 b1).

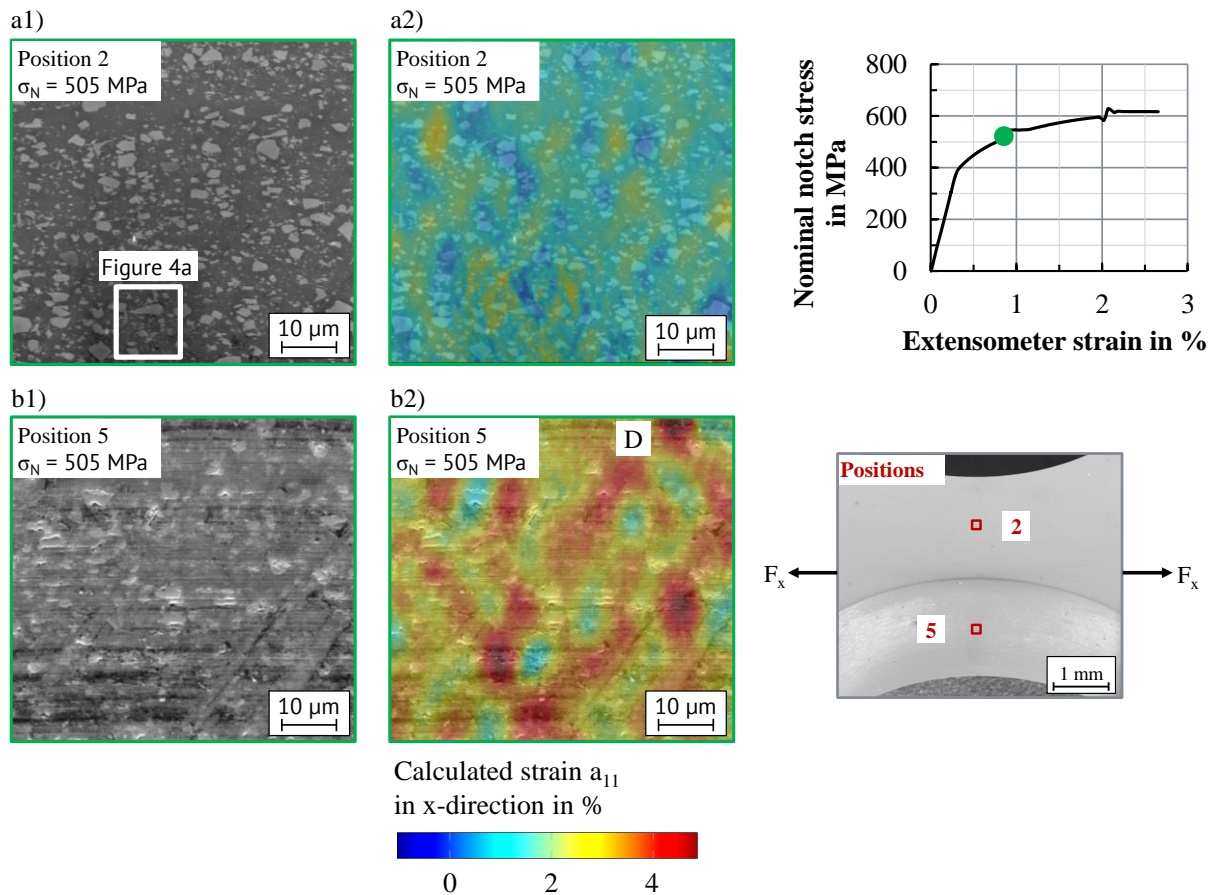


Figure 5: Calculated strain a_{11} in loading direction shown for AMC 217xe ($\alpha_K = 1.1$) at 505 MPa nominal notch stress; a) position 2, b) position 5

The calculated derivative $\partial_x u_1$ highlights local damages as described in chapter 3.4. The image analysis algorithm was applied to micrographs taken at position 2 and position 5 at 595 MPa nominal notch stress, i.e. larger plastic deformation than in Figure 5, but still well below elongation to failure. Hence, the load level considered in the image analysis shown in Figure 6 is between the already given results of Figure 4 (628 MPa) and Figure 5 (505 MPa). Figure 6 shows the results of the local damage detection at a) position 2 and b) position 5. Corresponding to Figure 4, the same slip marks (A), decohesions (B) and SiC particle cracks (C) are highlighted by sharply localized high values of the calculated derivative at this loading. Especially for the higher magnification of position 2 the described damage types are highlighted in good accordance by the calculated derivative in Figure 6 a2. The micro crack at position D in Figure 4 b is already open at this load level (see Figure 6 b1). This is also represented in Figure 6 b2 by the sharp gradient of the calculated derivative in contrast to the relatively smooth distribution in the surrounding areas.

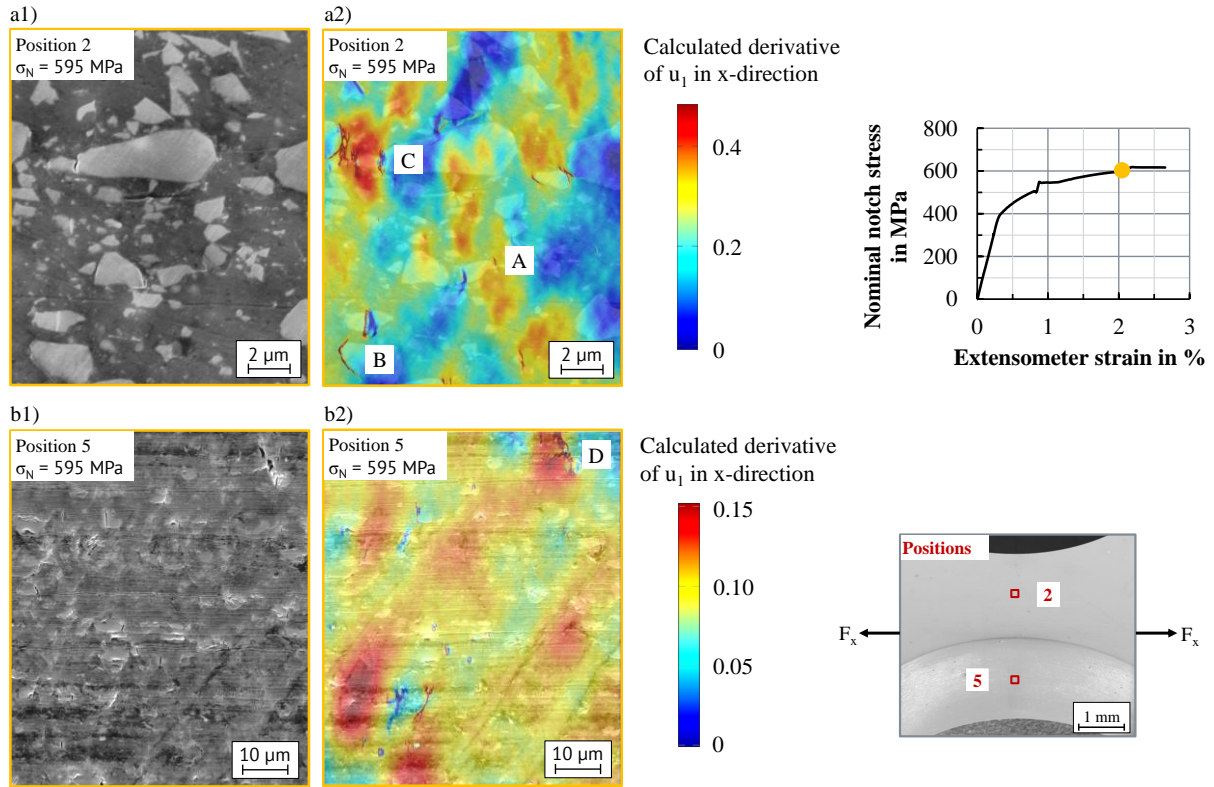


Figure 6: Highlighting of local damages by calculated derivative $\partial_x u_1$, shown for AMC 217xe ($\alpha_K = 1.1$) at 595 MPa nominal notch stress; a) position 2, b) position 5

Results of calculated strains a at 628 MPa nominal notch stress for AMC 217xe are given in Figure 7. For a better orientation within the micrograph, Figure 7 a shows again the higher magnified area of position 2 (see Figure 5 a1). Highest local strains a_{11} in loading direction concentrate within the aluminum matrix, see Figure 7 b. Negative values for the calculated lateral strain a_{22} perpendicular to the load axis correspond to a shrinkage transversely to loading direction within the aluminum matrix (Figure 7 c). Combining both results, purely elastic behavior and high stiffness of the SiC particles is confirmed by calculated strains around 0 % in both cases. Compared to the results of Figure 5 a2, an overall increase of calculated strains a_{11} is determined in Figure 7 b.

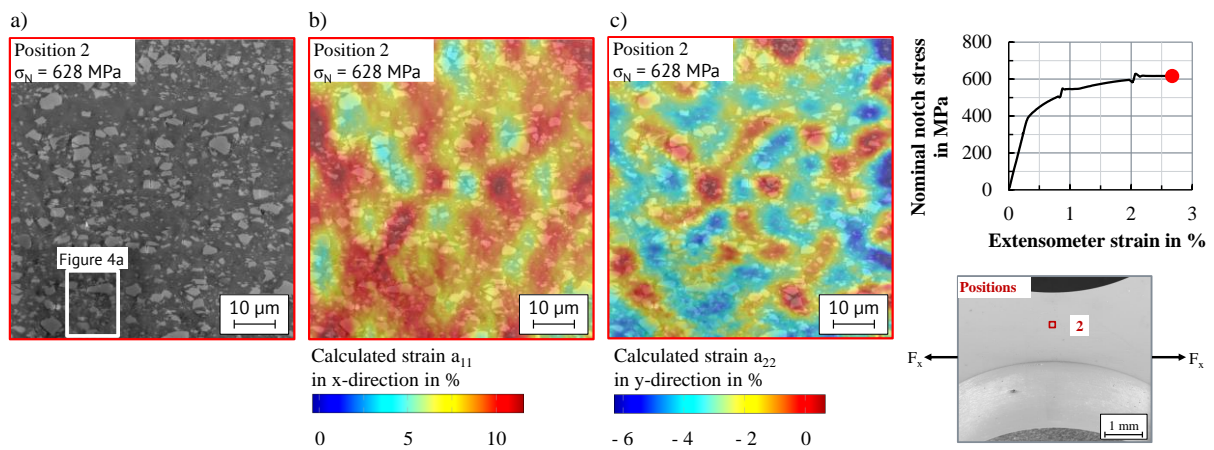


Figure 7: Calculated strain exemplarily shown for AMC 217xe ($\alpha_K = 1.1$) at 628 MPa nominal notch stress for position 2; a) SEM micrograph, b) strain a_{11} in loading direction, c) lateral strain a_{22}

It should be noted in this context that the mathematical algorithm currently neither features implementation of material properties nor includes detection of local phases. Nevertheless, the image analysis characterizes local deformation behavior of each phase according to a strong difference of Young's modulus of both single components by a factor of 6, see also Table 2.

A comparison of calculated strains a_{11} in loading direction at position 2 for specimen geometry $\alpha_K = 1.1$ of all AMC variants is summarized in Figure 8 for loading slightly above the macroscopic yield limit, corresponding to a measured extensometer strain of 0.5 % (Figure 8 d). The difference between the calculated results for AMC 217xe (Figure 8 a) and AMC xxfine217 (Figure 8 c) is rather small. A detailed view at Figure 8 a shows strain concentrations mostly within the aluminum matrix. This verifies the results given in Figure 7 for another experiment at the same material. The deformation localization is qualitatively similar in the AMC xxfine217 variant (Figure 8 c) for this loading at position 2. The micrograph of AMC xfine217 (Figure 8 b) shows significantly lower values although there are no microstructural damages visible at the same observation position as in the other AMCs (Figure 8 a and Figure 8 c). The future macroscopic crack paths documented after final failure of each specimen are highlighted in Figure 8 e. The artificial lines indicate the later crack path and visualize their distance to the observed position. As the crack path for AMC xfine217 is most far apart from the observed position 2, plastic deformation is less pronounced within this observed area. Therefore, the higher strain values on the local scale calculated by mathematical image analysis also indicate the influence of the global crack path at that early state of loading slightly above the yield limit. Furthermore, load redistribution caused by such cracks on local damage can be visualized especially for AMC 217xe in Figure 8 a where strain localization is pronounced in the observed area close to the future crack path.

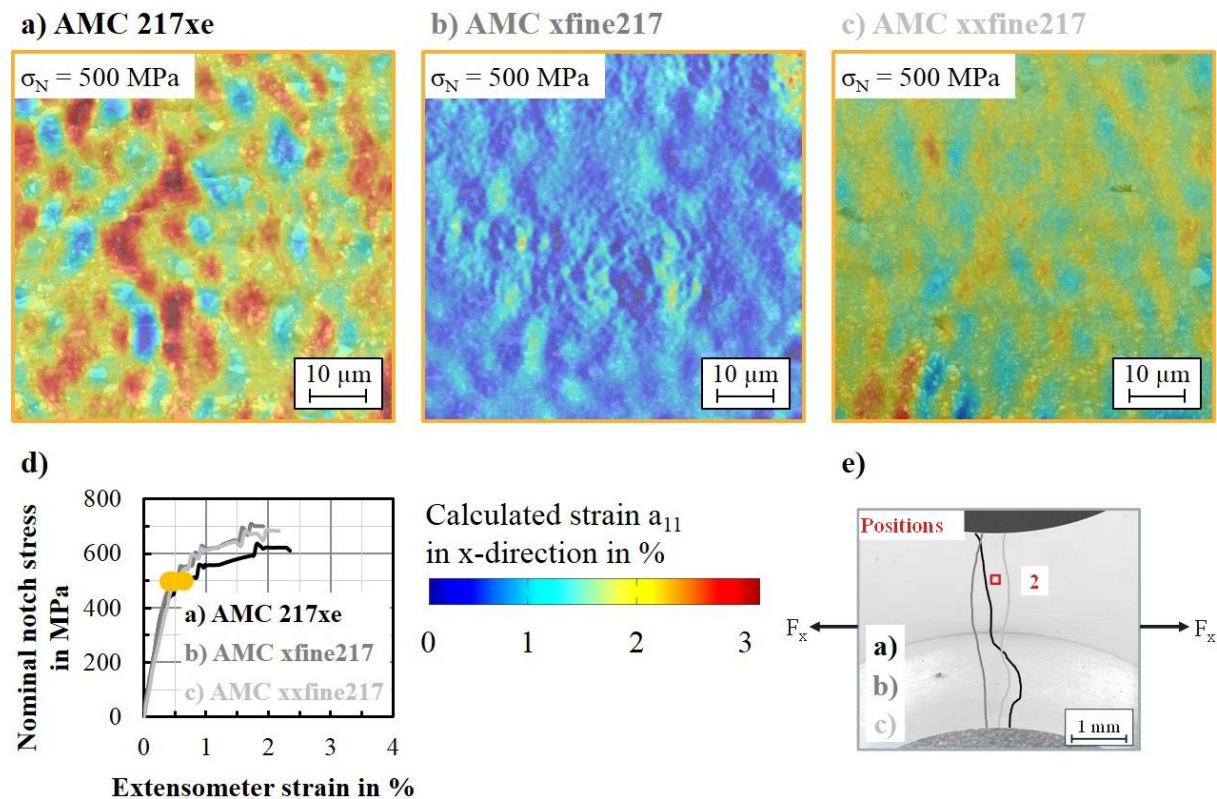


Figure 8: Calculated strain a_{11} at 500 MPa nominal notch stress ($\alpha_K = 1.1$) for a) AMC 217xe, b) AMC xfine217, c) AMC xxfine217, d) macroscopic measured stress-strain curve, e) macroscopic crack path for all AMC variants after failure

5 CONCLUSIONS AND OUTLOOK

The present study focuses on monotonic deformation and damage behavior of AMC reinforced by SiC particles with a nominal volume content of 17 %. Three AMC variants with nominal particle sizes from 0.3 μm to 3 μm were investigated. Ex situ monotonic tensile tests were performed to determine mechanical properties of all materials. Additionally, micro-mechanical tests on notched ($\alpha_k = 1.1$) flat samples were realized using an in situ tension-compression load frame mounted in a SEM. Micrograph sequences were determined under increasing mechanical load up to final failure on representative positions on the top surface and in the notch root. Mathematical image analysis was used to calculate the surface strain tensor from a reference image of the microstructure in the unloaded state at the same position with applied load. This technique allows a computation and visualization of the evolution of local displacements in the multiphase microstructure during mechanical loading with high spatial resolution and sensitivity.

The microstructural characterization of the initial state shows an alignment of the SiC particles along the extrusion direction for all AMC variants. SiC particle size only has a weak influence on the macroscopic Young's modulus determined by monotonic tensile tests according to DIN EN ISO 6892-1. Furthermore, with increasing SiC particle size a decrease of UTS is determined. In situ deformation tests underpin this trend for all investigated AMC versions. Different damage types clearly influence the surface deformation distribution: Slip marks occur within the aluminum matrix due to plastic deformation. Decohesions are initiated at the interface of SiC particles and aluminum matrix, followed by micro cracks inside the aluminum matrix. Finally also selected SiC particles crack under high load shortly before failure of the specimen. This general behavior is independent of the reinforcement particle size, but – as expected – the degree of damage localization increases with decreasing particle size. Onset of local damage is indicated in the local strain patterns derived by mathematical image analysis in a very early state of deformation, proving the developed image analysis approach to be much more sensitive in damage detection than conventional observation of SEM images. The comparison of all AMC variants shows similar results for calculated local strain fields of AMC 217xe and AMC xxfine217. The significantly lower values for AMC xfine217 are due to influences of stress redistribution caused by a macroscopic crack located relatively far from the position of local strain analysis. As a result, a cross-correlation of local deformation behavior based on mathematical image analysis with the macroscopic crack path of a specimen is possible.

ACKNOWLEDGEMENTS

Funding by the German Research Foundation (DFG) within the Research Training Group (GRK) 1932 "Stochastic Models for Innovations in the Engineering Sciences" at University of Kaiserslautern (Germany) is gratefully acknowledged by the authors.

REFERENCES

- [1] Hooker, J. A.; Doorbar, P. J.: Metal matrix composites for aeroengines, Bd. 16. In: Cantor, B.; Dunne, F.; Stone, I. C. (Ed.): *Metal and ceramic matrix composites*. Bristol : Institute of Physics Publ (2004), p. 725–731
- [2] Allison, J. E.; Cole, G. S.: Metal-matrix composites in the automotive industry: Opportunities and challenges. In: *JOM* 45 (1993), vol. 1, p. 19–24
- [3] Rawal, S. P.: Metal-matrix composites for space applications. In: *JOM* 53 (2001), vol. 4, p. 14–17
- [4] Ushio, U. Hayashi, T.: Application of MMC to automotive production engines. In: *Aluminium* 68 (1992), vol. 11, p. 989
- [5] Pai, B. C.; Rajan, T. P. D.; Pillai, R. M.: Aluminium matrix composite castings for automotive applications. In: *Indian foundry journal* 50 (2004), vol. 9, p. 30–39
- [6] Chawla, N.; Chawla, K. K.: *Metal matrix composites*. New York, NY: Springer (2006)

- [7] Suresh, S. (Ed.): *Fundamentals of Metal-Matrix Composites*. Burlington: Elsevier Science (2013)
- [8] Nishida, Y.: *Introduction to Metal Matrix Composites: Fabrication and Recycling*. Tokyo: Springer (2013)
- [9] Gribkov, A. N.: Composites of the aluminium - silicon carbide system. In: Fridlyander, J. N. (Ed.): *Metal Matrix Composites* : Springer-Science+Business Media, B.V. (1995), p. 440–486
- [10] Voorhees, P.; Spanos, G.: *Modeling Across Scales: A Roadmapping Study for Connecting Materials Models and Simulations Across Length and Time Scales: The Minerals, Metals & Materials Society* (2015)
- [11] Balle, F.; Eifler, D.; Fitschen, J. H.; Schuff, S.; Steidl, G.: Computation and Visualization of Local Deformation for Multiphase Metallic Materials by Infimal Convolution of TV-Type Functionals, Bd. 9087. In: Aujol, J.-F.; Nikolova, M.; Papadakis, N. (Ed.): *Scale Space and Variational Methods in Computer Vision*. Cham : Springer International Publishing (2015), p. 385–396
- [12] Balle, F.; Beck, T.; Eifler, D.; Fitschen, J. H.; Schuff, S.; Steidl, G.: Strain Analysis by a Total Generalized Variation Regularized Optical Flow Model. (2017)
- [13] Chawla, N.; Shen, Y.-L.: Mechanical Behavior of Particle Reinforced Metal Matrix Composites. In: *Advanced Engineering Materials* 3 (2001), vol. 6, p. 357–370
- [14] Materion Aerospace Metal Composites Limited: *SupremEX: Data Sheet*. (Farnborough, 28.05.2015)
- [15] You, C. P.; Thompson, A. W.; Bernstein, I. M.: Proposed failure mechanism in a discontinuously reinforced aluminum alloy. In: *Scripta Metallurgica* 21 (1987), vol. 2, p. 181–185
- [16] Milman, Y.; Chugunova, S. I.; Goncharova, I. V.; Chudoba, T.; Lojkowski, W.; Gooch, W.: Temperature dependence of hardness in silicon–carbide ceramics with different porosity. In: *International Journal of Refractory Metals and Hard Materials* 17 (1999), vol. 5, p. 361–368
- [17] Granta Design: *CES EduPack 2017*. Cambridge (2017)
(URL: <http://www.grantadesign.com/education>)
- [18] Evans, A.; Phaneuf, M. W.; Boyd, J. D.: Imaging damage evolution in a small particle metal matrix composite. In: *Journal of Microscopy* 196 (1999), vol. 2, p. 146–154
- [19] Kolednik, O.; Unterweger, K.: The ductility of metal matrix composites – Relation to local deformation behavior and damage evolution. In: *Engineering Fracture Mechanics* 75 (2008), vol. 12, p. 3663–3676
- [20] Liebchen, M.; Hübner, P.; Biermann, H.: In-situ-Zugversuche an Metall-Matrix-Verbundwerkstoffen. In: Degischer, H.-P. (Ed.): *Verbundwerkstoffe*. Weinheim, FRG : Wiley-VCH Verlag GmbH & Co. KGaA (2003), p. 183–188
- [21] Srivatsan, T. S.; Prakash, A.: The quasi-static fracture behavior of an aluminum alloy metal-matrix composite. In: *Composites Science and Technology* 54 (1995), vol. 3, p. 307–315
- [22] Unterweger, K.; Kolednik, O.: The local deformation behaviour of MMCs – an experimental study. In: *Zeitschrift für Metallkunde* 96 (2005), vol. 9, p. 1063–1068